

Civil Engineering Journal

(E-ISSN: 2476-3055; ISSN: 2676-6957)

Vol. 11, No. 09, September, 2025



Numerical Analysis of Ground Motion Topographic and Geological Effect: A Case Study of MOXI Platform

Shixing Zhao ¹6, Qirui Luo ^{1*}, Yuanxu Tang ¹, Jing Xia ¹, Yingmin Li ²6, Min Zhang ³

¹ Sichuan Provincial Architectural Design and Research Institute, Chengdu 610041, China.

² School of Civil Engineering, Chongqing University, Chongqing 400045, China.

³ School of Civil Engineering and Geomatics, Southwest Petroleum University, Chengdu 610500, China.

Received 26 May 2025; Revised 13 August 2025; Accepted 19 August 2025; Published 01 September 2025

Abstract

The ground motion amplification effect influenced by diverse topographic and geological conditions was investigated to enhance the seismic design standards for mountain structures. A comprehensive series of two-dimensional and three-dimensional numerical simulations was conducted. These simulations utilized idealized and real-world topographic models, meticulously considering various critical parameters, such as platform height, width, slope, surface angle, and soil properties. The results reveal that topographic and geological factors both significantly impact the ground motion amplification effect, with the maximum amplification factors frequently surpassing those stipulated by the current Chinese seismic code. Based on these findings, a refined and modified formula was developed for calculating the ground motion amplification factor that integrates the influences of height, width, slope, and geological conditions. The validity and feasibility of this modified formula were substantiated thoroughly through detailed comparisons between the actual observed values and the suggested values, demonstrating its potential to improve the safety and reliability of seismic design in mountainous regions substantially.

Keywords: Topographic Effect; Geological Effect; Ground Motion Amplification Factor; Platform Topography; Numerical Analysis.

1. Introduction

Earthquakes are common natural disasters that cause great damage to human societies and economies [1–4]. Ground motion is the vibration of the Earth's surface at the time of an earthquake, and its intensity and frequency properties have an important influence on the seismic resistance of structures and the extent of seismic hazards. Topography and geology are important factors in the propagation of earthquake waves [5, 6], and their study is important for understanding the generation and propagation mechanisms of ground motion, assessing the risk of earthquake disasters, and designing earthquake-resistant buildings.

Topography conditions are an important factor in improving the ground motion. The related definition about topographic effect was given by the Network for Earthquake Engineering Simulation (NEES) [7]: "Focusing, defocusing, diffraction and scattering of seismic waves by irregular surface geometry, affecting amplitude, frequency and duration of ground motion compared to flat ground conditions." Numerous studies have been conducted to quantify the topographic amplification effect. Pelekis et al. [8] studied the Achaia-Ilia (Greece) 2008 Ms 6.4 earthquake and performed a simulation analysis. The results demonstrated that the spectral amplification in the period range of T =

^{*} Corresponding author: luoqiruilqr@126.com



doi http://dx.doi.org/10.28991/CEJ-2025-011-09-01

© 2025 by the authors. Licensee C.E.J, Tehran, Iran. This article is an open access article distributed under the terms and conditions of the Creative Commons Attribution (CC-BY) license (http://creativecommons.org/licenses/by/4.0/).

0.15–0.35 s ranged from 12% to 18%. Dhabu et al. [9] researched the influence of Himalayan topography on earthquake ground motion, as shown in Figure 1. The results show that the maximum amplifications of horizontal and vertical velocity are 3.2 and 3.7, respectively. Hartzell et al. [10] studied the influence of topography on ground motion using a year of measurement records from Poverty Ridge on the east side of the San Francisco Bay Area, California. The data showed a ridge-crest amplification of a factor of 3–4 at a fundamental resonance of approximately 0.5–1.0 Hz

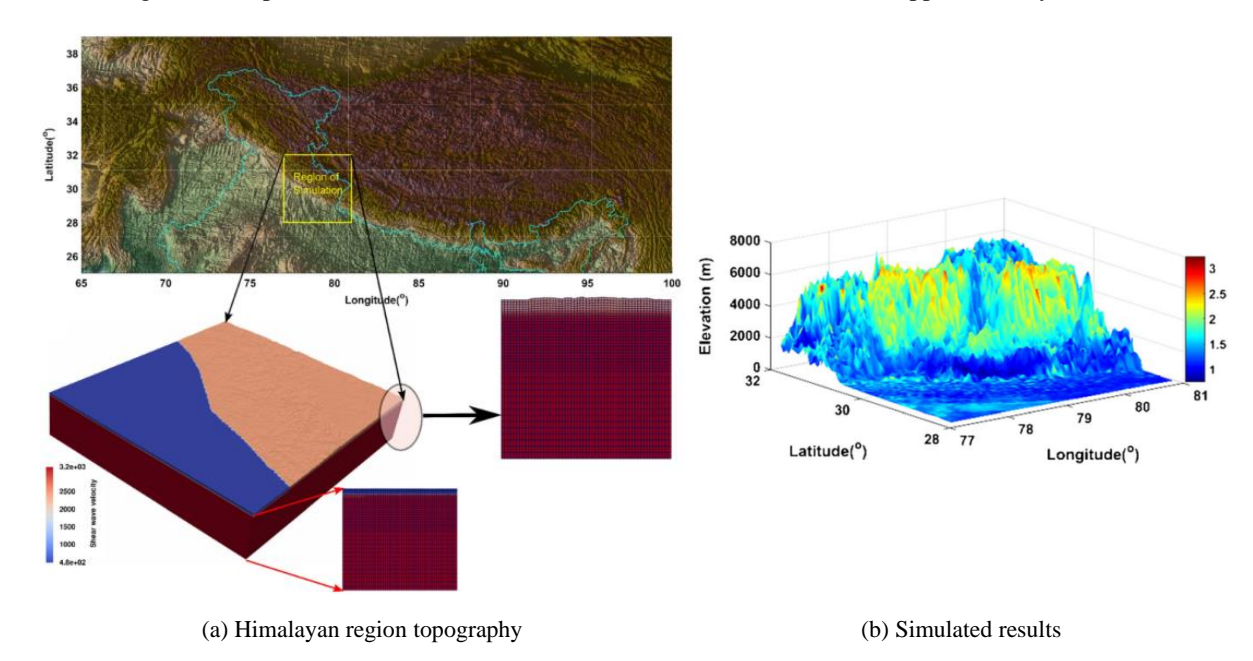


Figure 1. Himalayan region topography and simulated results [9]

Another important factor affecting ground motion is geological conditions. Luo et al. [11] investigated the geological amplification effect in the Qiaozhuang region in Sichuan Province, China. They found that the amplification factor was less than 3, considering only topographic features, and much lower than 6 for the monitoring data. The results agreed well with the monitoring data when geological features were considered in the analysis model. Glinsky et al. [12] reported a simulated analysis that considered topographic and geological site effects. The results showed that heterogeneous models had the strongest amplifications. Hough et al. [13] investigated the structural damage caused by the 2010 Haiti earthquake. They pointed out that, topographic and geological amplification contributed significantly to the damage in the district of Petionville, south of central Port-au-Prince. Shen et al. [14] parametrically explored the combined effects of topography and stratigraphy of layered rock slopes on seismic amplification. The results indicated that the maximum amplification factor was 7.4.

Although much research on the site effect has been completed, the object of these studies was the specified site condition. It was difficult to determine amplification factors from the results when the structural sites had different topographies. According to the literature, structural design in mountainous areas is difficult. The Chinese seismic code [15] provides the reference ground motion amplification factor at the edge of a locally raised topography when designing mountain structures, as listed in Table 1. The maximum topographic and geological effect amplification factor in the seismic code is 1.6. Further investigations are necessary to determine whether this value is safe. In addition, the lack of systematic research on the ground motion amplification factor has made it difficult to provide guidance for structural design in mountainous regions.

Table 1. Ground motion amplification factor at the edge of local raised topography

Raised topography	Nonrock layer	H<5	5≤H<15	15≤H<25	H≥25	
height (m)	Rock layer	H<20	20≤H<40	40≤H<60	H≥60	
	H/L<0.3	1.0	1.1	1.2	1.3	
Average slope	0.3≤H/L<0.6	1.1	1.2	1.3	1.4	
(H/L)	0.6≤H/L<1	1.2	1.3	1.4	1.5	
	H/L≥1	1.3	1.4	1.5	1.6	

Note: H is topographic height. L is topographic width. H/L is topographic slope.

Therefore, in this study, a real topographic effect case was used first to show the incompleteness and imperfection of the related regulations in the Chinese seismic code. Then, a two-dimensional (2D) ideal platform model was established, and ground motion was systematically studied by altering the topographic and geological parameters of the

platform topography. Subsequently, a three-dimensional (3D) real MOXI topography model was established to analyze the acceleration time-history curve and the ground motion of the MOXI platform. Finally, the results of this study suggest that the value of the seismic amplification factor should be modified to provide a reference for the seismic design of buildings in areas with unfavorable topography and geology.

2. Ground Motion Amplification Effect

On September 5, 2022, an Ms 6.8 earthquake struck Luding County (Figure 2), Sichuan Province, southwest China, where the damage to the town of MOXI was the most severe. The topography of MOXI is a platform with a height difference of approximately 130 m, as shown in Figure 3. The peak accelerations of the east-west and north-south Ms 6.8 earthquake waves in MOXI were 634.06 and 482.55 cm/s², respectively. Many studies have investigated the damage in the town [16–20]. The ground motion amplification factor of the MOXI platform should be determined as 1.6 according to the Chinese seismic code. However, in the disaster survey, the same structures with an amplification factor of 1.6 had significantly different earthquake damage phenomena, of those to which the MOXI museum (framed structure) were the most pronounced

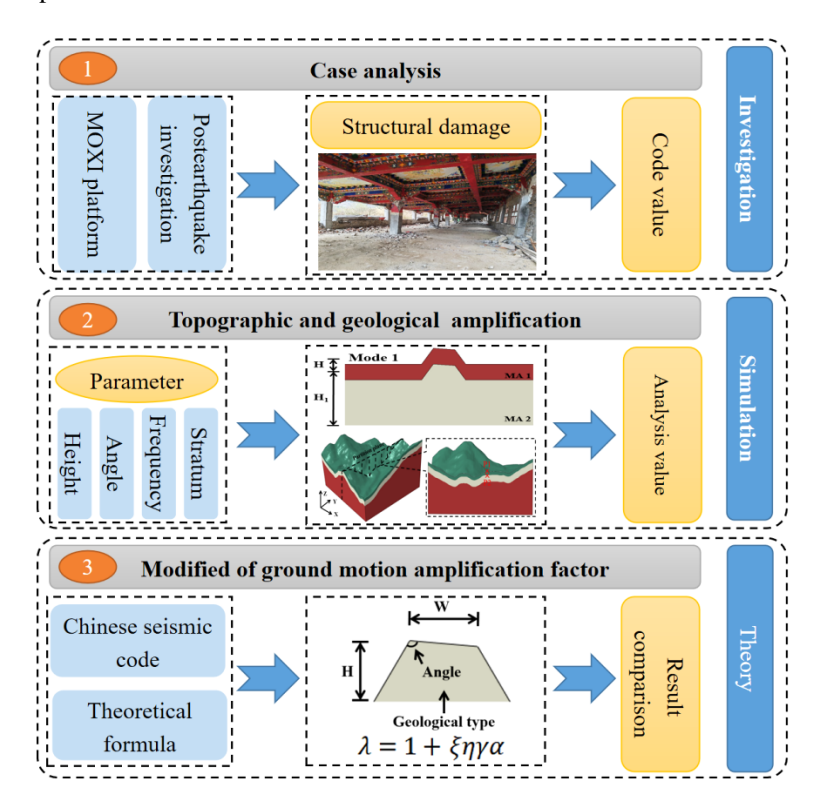


Figure 2. Flowchart of the research methodology

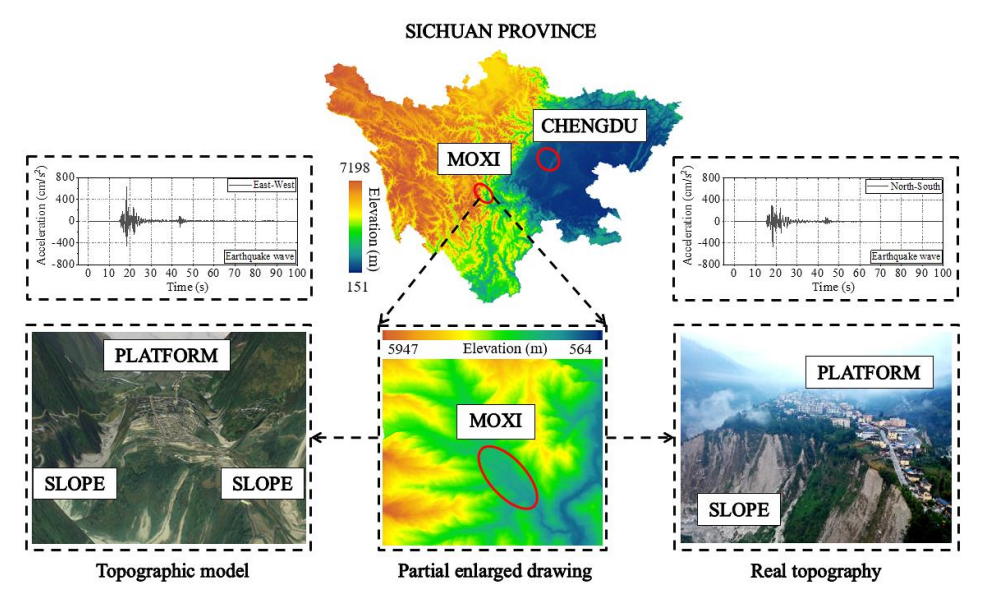


Figure 3. MOXI topography

The MOXI museum was located at the edge of the platform, and the structure was symmetrical, as shown in Figure 4. During the earthquake, although the topographic amplification factor of the structural design for the MOXI museum was 1.6, the damage conditions of the structures near and away from the slope were significantly different. Buildings near the slope were close to collapsing, with severe damage to the frame columns, whereas buildings farther from the slope suffered minor damage, with only a few fully infilled walls collapsing. The seismic responses of the structures with the design values defined by the Chinese seismic code were significantly different under the seismic action. Therefore, the definition of the code was incomplete, and the ground motion amplification factor near the slope should be defined using other values. To provide a reference for the seismic design of mountain buildings, the effects of topographic and geological parameters on the ground motion should be studied systematically.

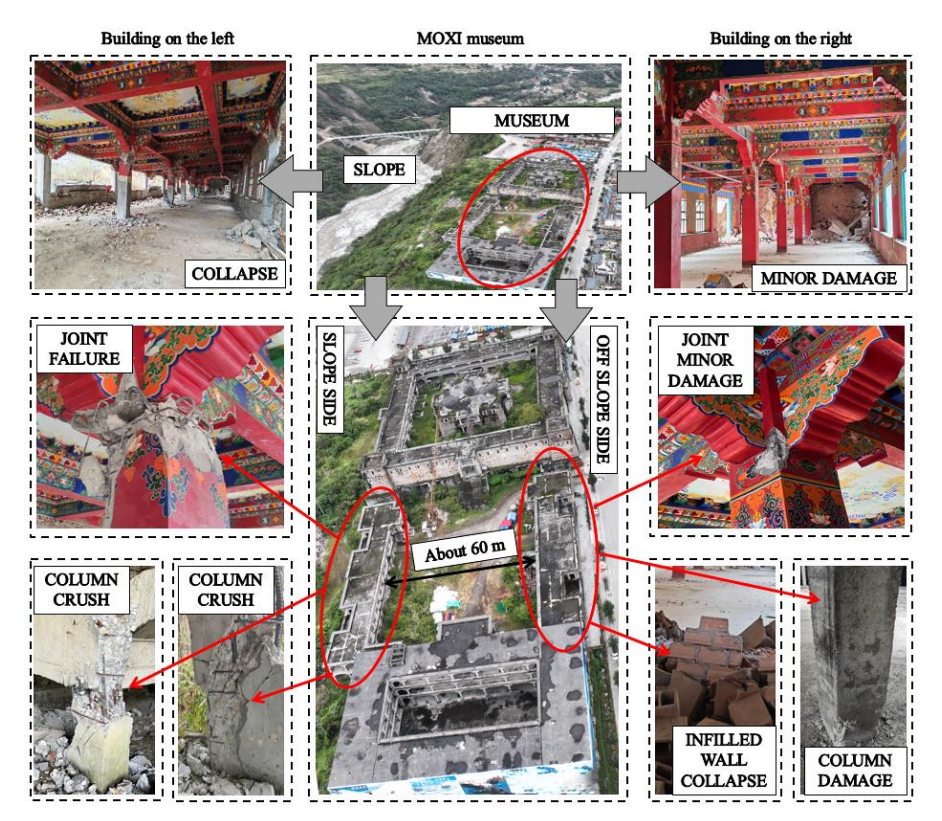


Figure 4. Different damage conditions of MOXI museum

3. Topographic Amplification Effect of 2D Simulation

3.1. Simulation Established of Ideal Platform

Platform topography is a common mountain building site, and its topographic effect should be researched specifically. The platform was simplified to an ideal trapezoidal topography, as shown in Figure 5. The element type in the simulation was CPS4R. The viscoelastic artificial boundary condition is a common method for simplifying an infinite foundation into a finite foundation [21–23]. The principle of the viscoelastic artificial boundary condition was to set the stiffness and damping springs to simulate the interaction between infinite and finite foundations. Elimination of the reflection interference of seismic waves was its other function. The stiffness and damping coefficients were calculated using Equations 1 to 4. Because this study focused mainly on the application of the viscoelastic artificial boundary method, the actual formulas and derivation processes are not provided. The derivation has been described previously [24].

$$k_{\rm n} = \alpha_{\rm n} \frac{G}{R} \tag{1}$$

$$d_{\rm n} = \rho C_{\rm s} \tag{2}$$

$$k_{t} = \alpha_{t} \frac{G}{R} \tag{3}$$

$$d_{\rm t} = \rho C_{\rm p} \tag{4}$$

where α_t and α_n are the tangential and normal viscoelastic artificial boundary parameters, respectively, C_s and C_p are the velocities of S- and P-waves, respectively. G and ρ are the shear modulus and density of foundation media, and R is the distance from the wave source to the artificial boundary. The earthquake wave input can be realized using the

equivalent load method [25]. However, because the influence of geological properties on the ground motion was investigated and the equivalent load method could not consider the difference between geological stratifications, the equivalent load method was not applied in this study. To explore the validity of the simulation, a specimen from the literature [26] was used for comparison. The specimen had a rock—soil mixture topography, the soil properties of which are listed in Table 2. The comparison between the simulation and literature is shown in Figure 6, where the maximum accelerations of the simulation and literature are 2.1 and 2.25 m/s², respectively. The difference is 0.12 m/s², indicating that the simulation method and properties are valid and can be used to study topographical and geological effects.

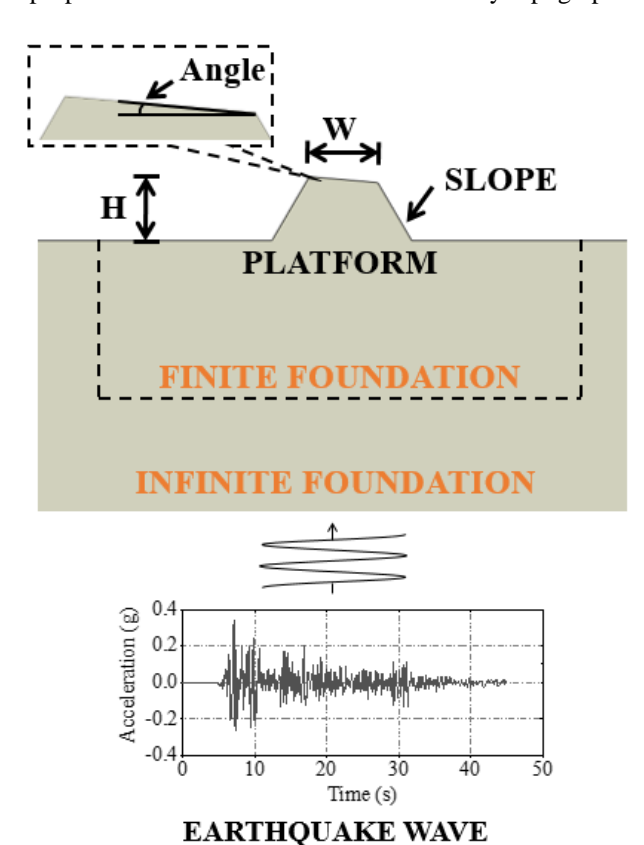


Figure 5. Ideal platform topography

Table 2. Soil properties [26]

Material parameter	Value
Density (kg/m³)	1830
Damping (%)	0.2
Friction angle (°)	41
Dilation angle (°)	4
Young's modulus (kPa)	2.391e5
Poisson's ratio	0.25
Shear wave velocity (m/s)	280

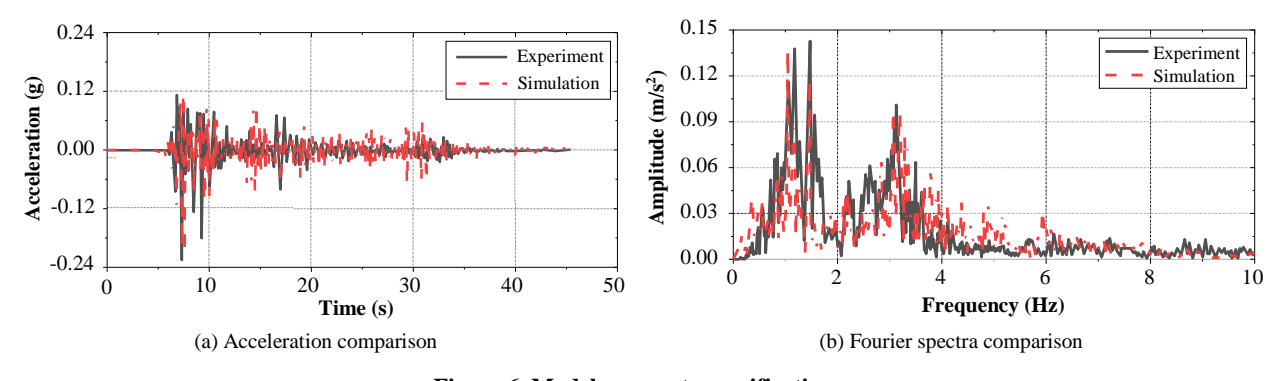


Figure 6. Model parameter verification

3.2. Coupled Effects of Platform Height and Width

The height and width were the main parameters of the topographic fluctuations of the MOXI platform (as shown in Figure 7); therefore, the focus was on the coupling effect of the height and upper surface width of the platform on the ground motion. The topographic width and height were 50 m, 100 m, 150 m, and 200 m. The slope and angle were 45° and 5°. The parameters are shown in Figure 5. The specimens were named "H-W." The geological conditions were determined to be uniform. The ground motion amplification factor was defined as the ratio of the peak acceleration of the platform surface to the peak acceleration of the input waves.

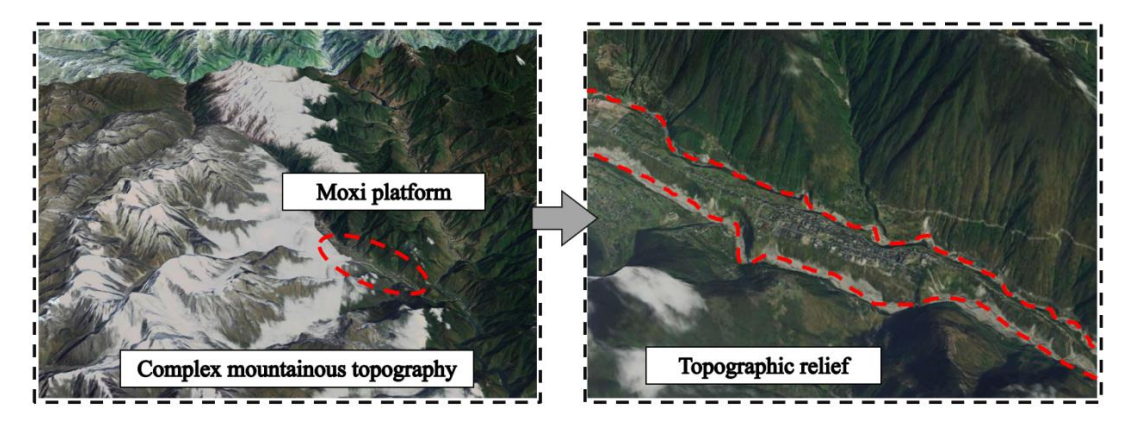


Figure 7. MOXI topography

Figure 8 shows the simulation results. For the slope on both sides of the platform, the ground motion amplification factor may have been be less than 1 because of the damping and vibration performance of the platform itself. However, as height increased, the influence of topographic effects on ground motion became more significant, and the ground motion amplification factor showed a rapidly increasing trend. For the upper surface of the platform, there was a clear fluctuation in the change in the ground motion amplification factor. The maximum ground motion amplification factors of some platform sections were not at the highest point (left upper surface endpoint) but in the middle. For example, the ground motion amplification factors of specimens 200-150 at the left endpoint and middle upper surface were 1.87 and 2.64, respectively. In addition, according to the Chinese seismic code [15], the maximum ground motion amplification factor was 1.6. However, the simulation results showed that the ground motion amplification factor of the platform could exceed 2.0. It can be observed that the value in the Chinese seismic code did not ensure the safety of the platform structure.

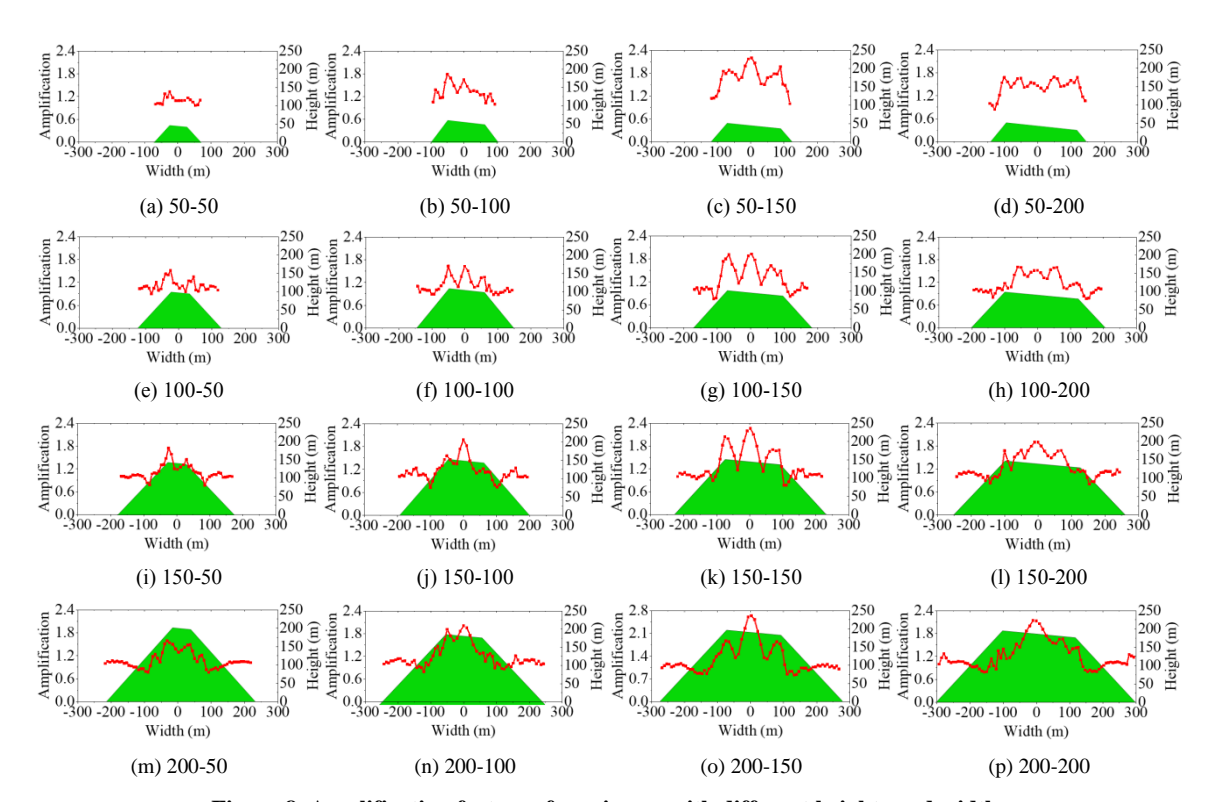


Figure 8. Amplification factors of specimens with different heights and widths

A spectral analysis was performed to determine the distribution of the maximum magnification of the platform topography. Fourier transform was performed on the time-history curve of each point. The frequency corresponding to the maximum amplitude of the wave was defined as the base frequency (BF), and the IBF represents the frequency corresponding to the maximum amplitude of the input wave. Figure 9 shows the acceleration time-history curves and Fourier spectra of specimens 200-150 and 50-50. The base frequency of the input wave was 1.31 Hz, which is denoted as BF in Figure 9. For specimen 200-150, the BFs of the middle point and endpoint were both 1.46 Hz, whereas the amplitudes were 0.103 and 0.139, respectively. In addition, the left endpoint was more sensitive to low frequencies (less than 1.31 Hz) than was the middle point. For specimen 200-50, when the frequency was less than 2 Hz, the left endpoint of the upper surface had an acceleration spectral curve similar to that of the middle point. When the frequency exceeded 2 Hz, the acceleration amplitude of the endpoint was more evident; thus, the topographic effect was more significant at the endpoint of the upper surface.

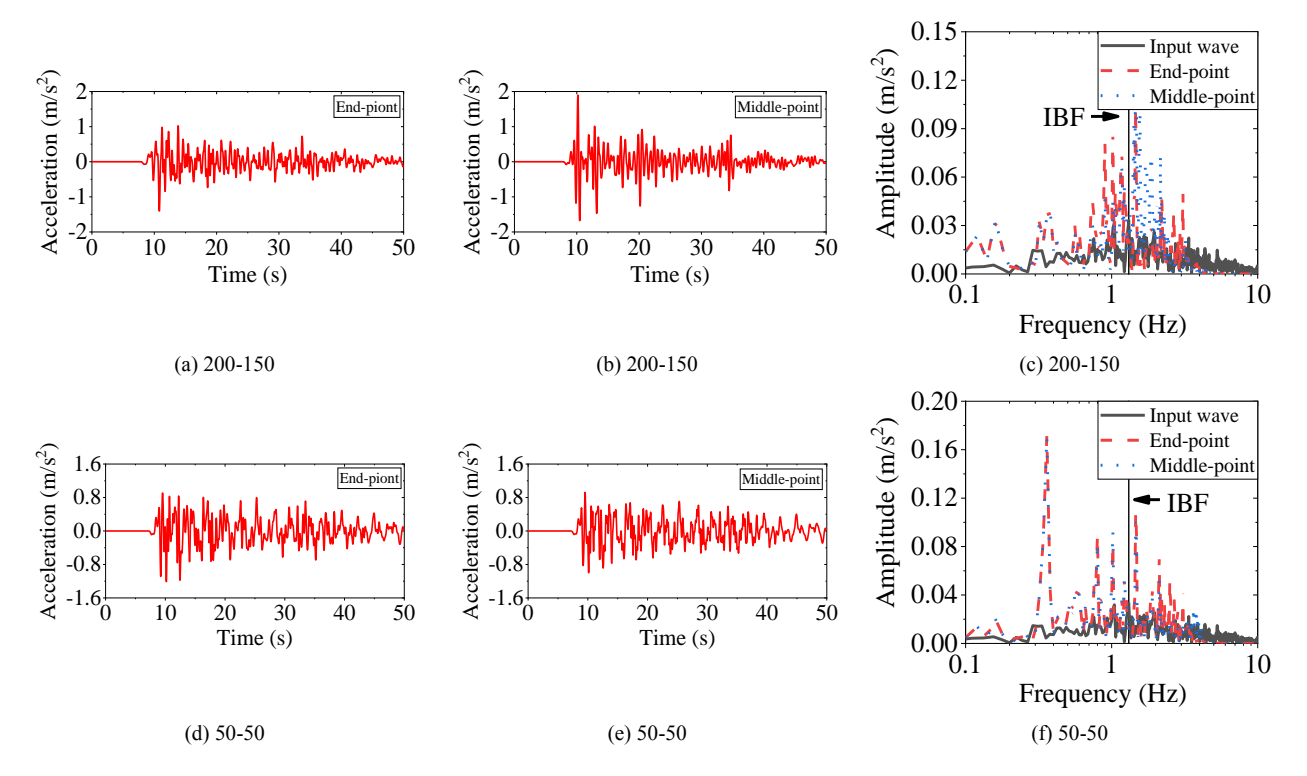


Figure 9. Acceleration time-history curves and Fourier spectra

3.3. Coupled Effect of Topographic Slope and Platform Surface Angle

In addition to the topographic height and width, the topographic slope and inclination angle of the upper surface of the MOXI platform are also important parameters affecting the topographic effect. Figure 10 shows the analysis results of the specimens with different topographic slopes and inclination angles of the upper surface, where the topographic height and width were 100 and 100 m, respectively. The specimens were named "Slope-Angle." The ground motion amplification factor had few changes with the increase of the upper surface angle when the slope was less than 60°. When the slope was equal to 60°, the maximum ground motion amplification factor increased with increasing surface angle, such as 2.27 for specimen 60-2.5 and 2.85 for specimen 60-10. In addition, the distribution of the maximum ground motion amplification factor was different in this group of specimens. When the slope was below 60°, the peak was distributed in the middle of the surface. When the slope was 60°, the peak appeared at the left endpoint of the upper surface. Spectral analysis was performed to explore the cause.

Figure 11 shows the acceleration time-history curves and Fourier spectra of specimens 30-2.5 and 60-10 at the left endpoint and middle point. For specimen 30-2.5, the acceleration peaks of the left endpoint and middle point were 1.24 and 1.65 m/s², respectively. From the Fourier spectrum of specimen 30-2.5, the main difference between the left endpoint and middle point was that the middle point had a higher acceleration amplitude when the frequency was greater than 3 Hz. This indicates that the topographic effect of the middle point was more pronounced. Hence, the seismic response at the middle point was more violent than that at the endpoint. For specimen 50-50, at the same frequency, the acceleration amplitude of the endpoint was higher, which made the seismic response of the endpoint more pronounced.

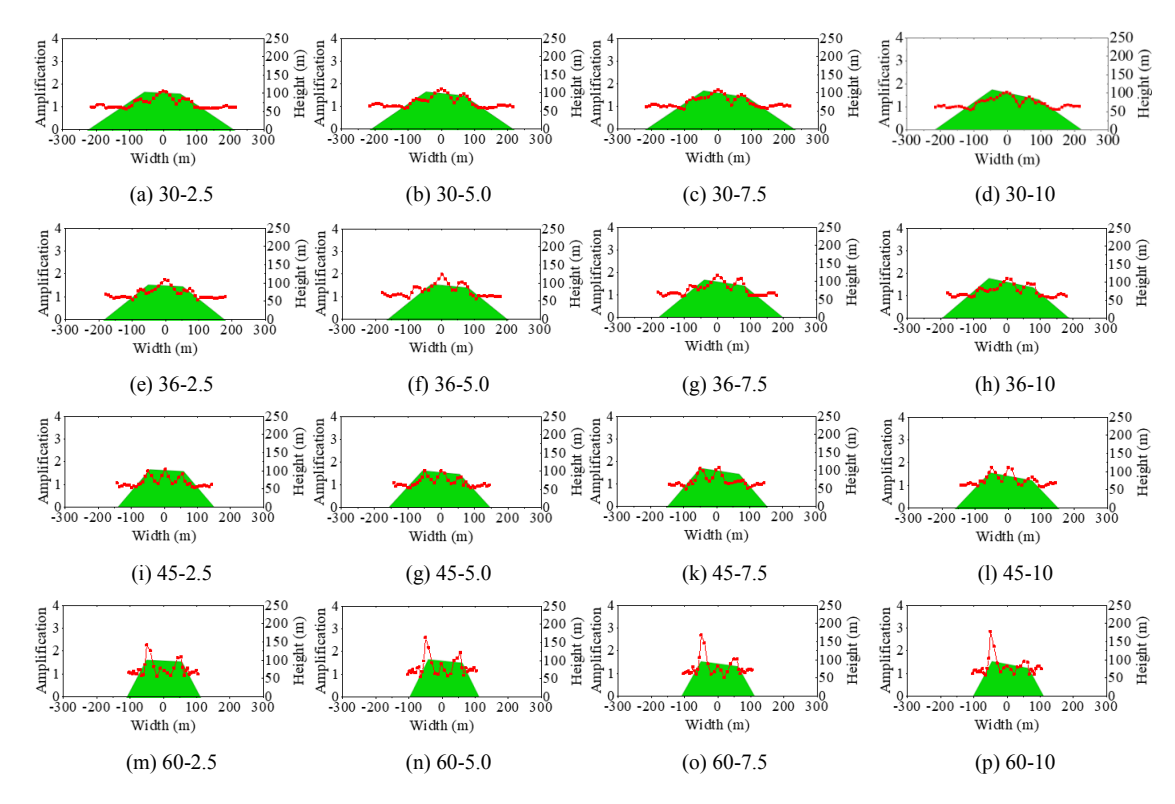


Figure 10. Amplification factors of specimens with different slopes and surface angles

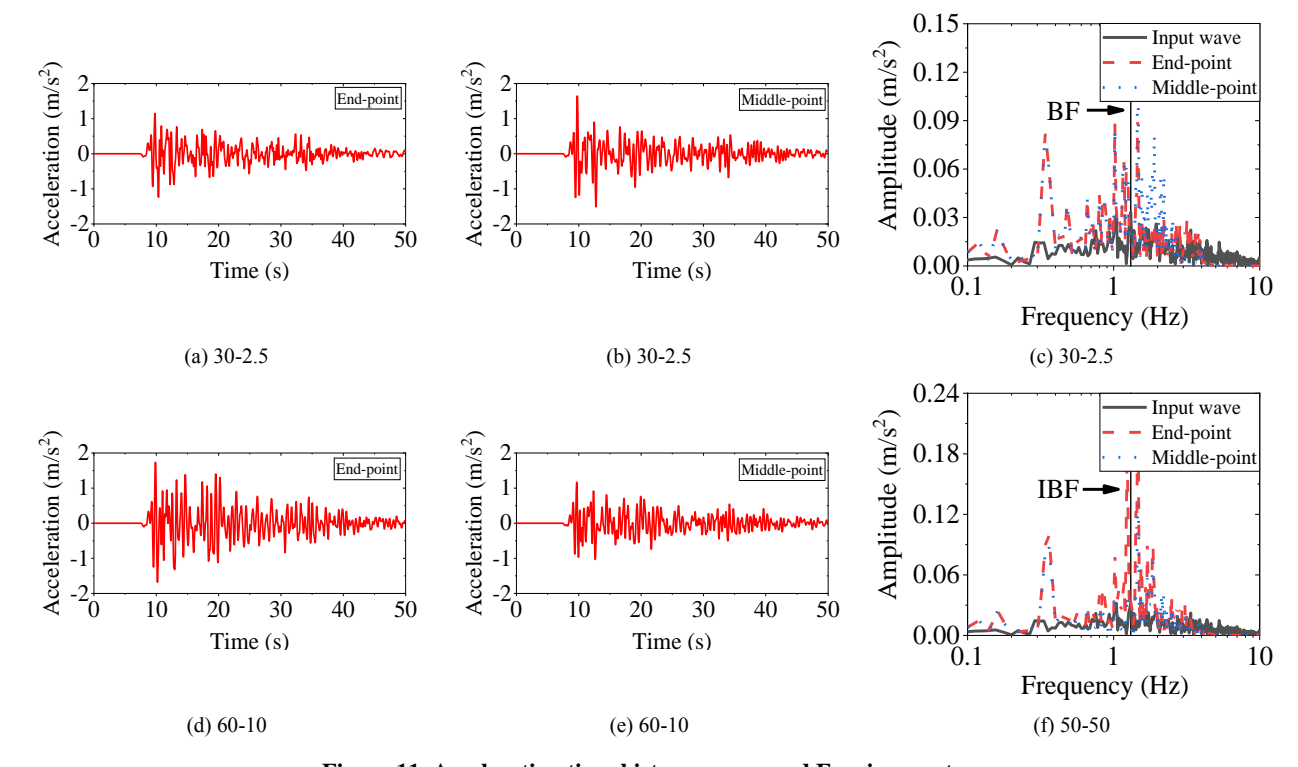


Figure 11. Acceleration time-history curves and Fourier spectra

4. Geological Amplification Effect of 2D Simulation

4.1. Simulation Established of Ideal Platform with Different Geological Layers

In recent decades, many simulations have been conducted, and it has been shown that simply accounting for topographic effects cannot reflect the amplification of ground motion objectively. Researchers have realized that ignoring geological soil conditions leads to underestimating the intensity of ground motion and that geological and topographic amplifications are not simple superposition relations [27]. Therefore, it is necessary to consider the changes of different geological layers in the modeling. Based on the actual drilling results of the MOXI topography, shown in

Figure 12, the soil is primarily a rock—soil mixture with a depth of more than 100 m. Because of gravity, the soil is not uniformly distributed. To facilitate the modeling, it was assumed in this study that the undersurface soil is divided into two layers. The soil parameters remain consistent within the depth range of (0, H). Within the range of (H, H+H1), the soil parameters change, as shown in Figure 13. The viscoelastic artificial boundary of the corresponding geological layers should also vary with the variations of soil properties.



Figure 12. Geological exploration results (drilling depth: 100 m)

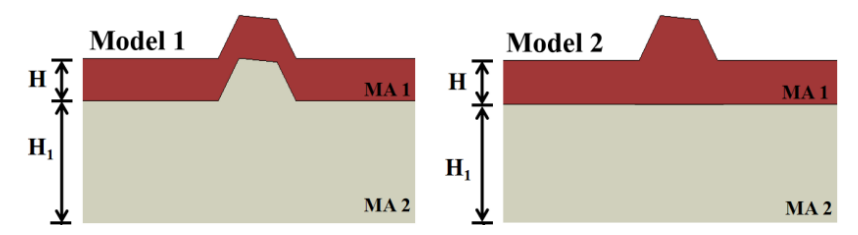


Figure 13. Different soil shapes

4.2. Couples Effect of Soil Depth and Properties with Two Geological Layers (Mode 1)

The depth of the geological layers and the soil properties clearly affect the propagation of seismic waves; therefore, these two factors were selected for analysis. Table 3 shows the properties of the different soil layers, with the main variable being the soil properties of the second geological layer. The topographic basis of the platform included a 100-m height, 100-m upper surface width, 45° slope, and 5° upper surface angle. The specimens were called "SD.MA," where SD and MA represented soil depth and soil material type. Figure 14 shows the ground motion amplification factor of the specimen with the geological shape of Mode 1. As the results show, for the geometrical shape of Mode 1, the influence on the ground motion amplification coefficient was small when the depth of the geologic layer was less than 200 m. However, the influence of the soil properties on the ground motion was significant. Taking four specimens with H = 100 m as an example, the ground motion amplification factors of the left endpoint (X-axis coordinate: -50 m) were 1.37, 1.61, 2.16, and 2.12. The maximum effect of soil properties was 1.58 times, indicating that considering only topographical effects does not reflect the ground motion amplification phenomenon objectively.

Soil properties Material Young's modulus P-wave velocity S-wave velocity Density Poisson's ratio E (kPa) ρ (kg/m³) $V_{\rm P}$ (m/s) Vs (m/s) 2.391e5 323.3 228.6 0.25 MA1 1830 0.25 MA2-1 1.1955e5 228.6 161.7 1830 MA2-2 2.391e5 323.3 228.6 1830 0.25 MA2-3 280.0 1830 0.25 3.5865e5 396.0 4.782e5 457.2 323.3 1830 0.25 MA2-4

Table 3. Soil properties

Notes: P-wave velocity was equal to $((\mu + 2*G)/\rho)^{0.5}$; S-wave velocity was equal to $(G/\rho)^{0.5}$; G was shear modulus and was equal to $0.5*E/(1+\mu)$.

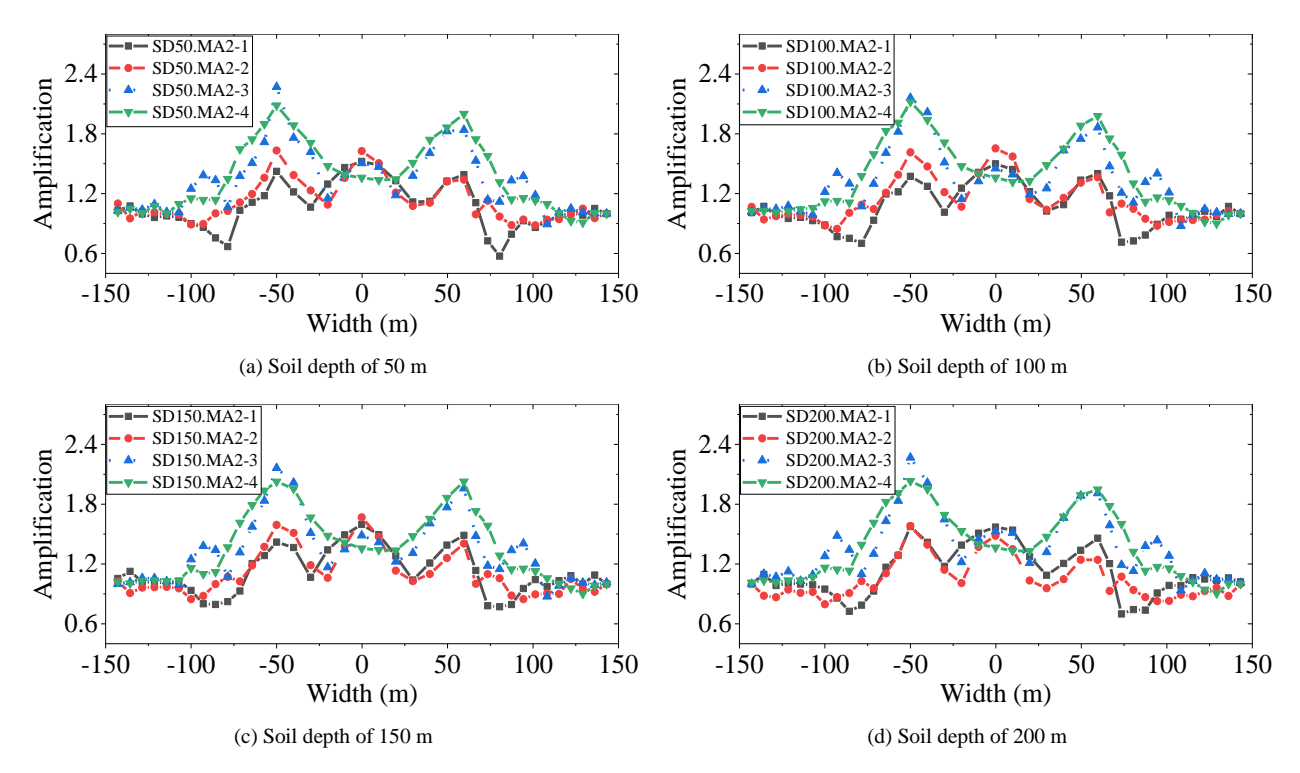


Figure 14. Ground motion amplification factor of specimen with soil shape of Mode 1

Spectral analysis was performed on four specimens with H = 100 m. Figure 15 shows a comparison of the acceleration spectra between the input wave and the endpoint of the upper surface. The topography had a significant amplification effect on the ground motion, which was more pronounced at frequencies in the range 0.1-3 Hz. As the elastic modulus of the second soil layer increased, the acceleration amplification at each frequency became more dispersed from the base frequency. For SD100.MA2-1, because the elastic modulus of the second-layer soil was lower than that of the first-layer soil, high-frequency waves (1.3-3) Hz were filtered out during seismic wave propagation. Therefore, the acceleration amplification was mainly concentrated on the low-frequency wave (0.1-1.3) Hz, where 1.3 Hz was the base frequency of input wave. This phenomenon changed as the elastic modulus of the second-layer soil increased. The amplification of the acceleration amplitude gradually extended to higher frequencies, thereby increasing the seismic response of the platform topography.

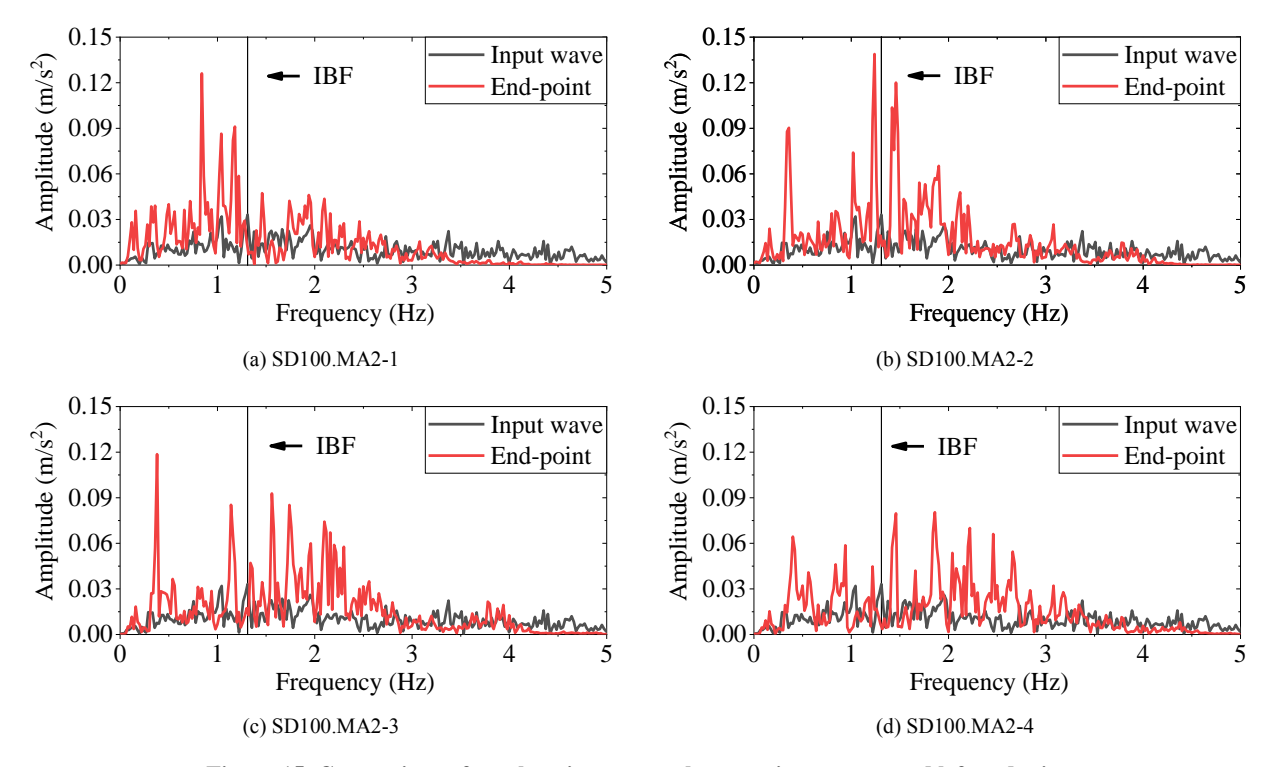


Figure 15. Comparison of acceleration spectra between input wave and left endpoint

4.3. Coupled Effect of Soil Depth and Properties with Two Geological Layers (Mode 2)

Based on the soil parameters described in Section 4.2, the shape of the soil layer was further altered, and an acceleration time-history analysis was performed. Figure 16 shows the ground motion amplification factor of the platform surface. For this soil layer shape, the soil layer depth had little influence on the ground motion amplification factor. However, the contact between different soil layers had an obvious influence on the propagation of earthquake waves. Compared with the soil layer of Mode 1, when the second geological layer had a lower elastic modulus, the ground motion amplification factor of the surface increased significantly. For example, the maximum surface ground motion amplification factor of specimen SD100.MA2-1 with geological layers of Modes 1 and 2 were 1.37 and 1.83, respectively, with an increase in amplitude of 33.6%. In contrast, the ground motion amplification factor was significantly reduced when the second layer had a higher elastic modulus. For example, the maximum surface ground motion amplification factors of specimen SD100.MA2-4 with soil layers of Modes 1 and 2 were 2.12 and 1.81, respectively, with a reduction amplitude of 33.6%. This might be because the different soil layers in Mode 2 were better able to transmit low-frequency waves, whereas soil layers with smaller elastic modes were more sensitive to lowfrequency waves, leading to a significant increase in their ground motion amplification factor, as shown in Figure 17. Conversely, soil layers with a higher elastic modulus were more sensitive to high-frequency waves; however, the shape of the soil layers in Mode 2 was less sensitive to high-frequency waves. Therefore, there was a difference in the ground motion amplification factor. To verify this hypothesis, a spectral analysis was performed.

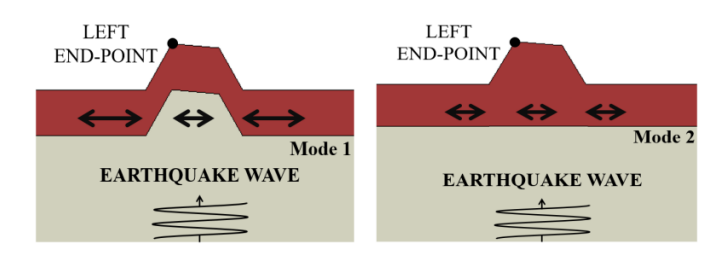


Figure 16. Interaction between different soil layers

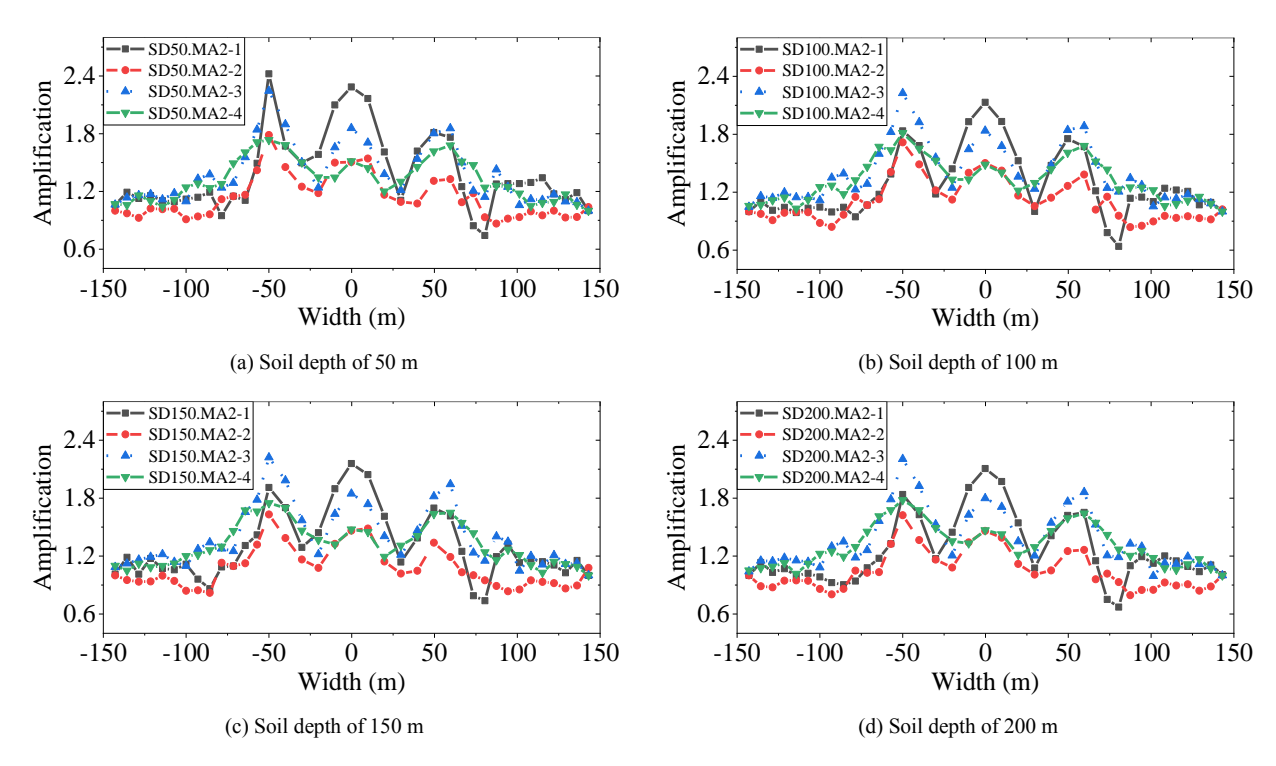


Figure 17. Ground motion amplification factor of specimen with soil shape of Mode 2

Figure 18 shows the acceleration spectral curves at the left endpoints of the four platforms with a soil layer depth of 100 m. For specimen SD100.MA2-1, the platforms with soil layer shapes of Modes 1 and 2 had the largest acceleration amplitude at a frequency of 0.84 Hz—0.126 and 0.251 m/s², respectively, with an amplitude increase of 99.2%. At a frequency of 2.5 Hz, the acceleration amplitudes were 0.018 and 0.011, indicating that the soil layer shape of Mode 2 was more sensitive to low-frequency waves. As the elastic modulus of the second soil layer increased, the spectral curve showed a gradual shift in the acceleration amplitude amplification region from low to high frequencies, indicating that specimen SD100.MA2-4 was more sensitive to high-frequency waves. Overall, this was consistent with previous speculation.

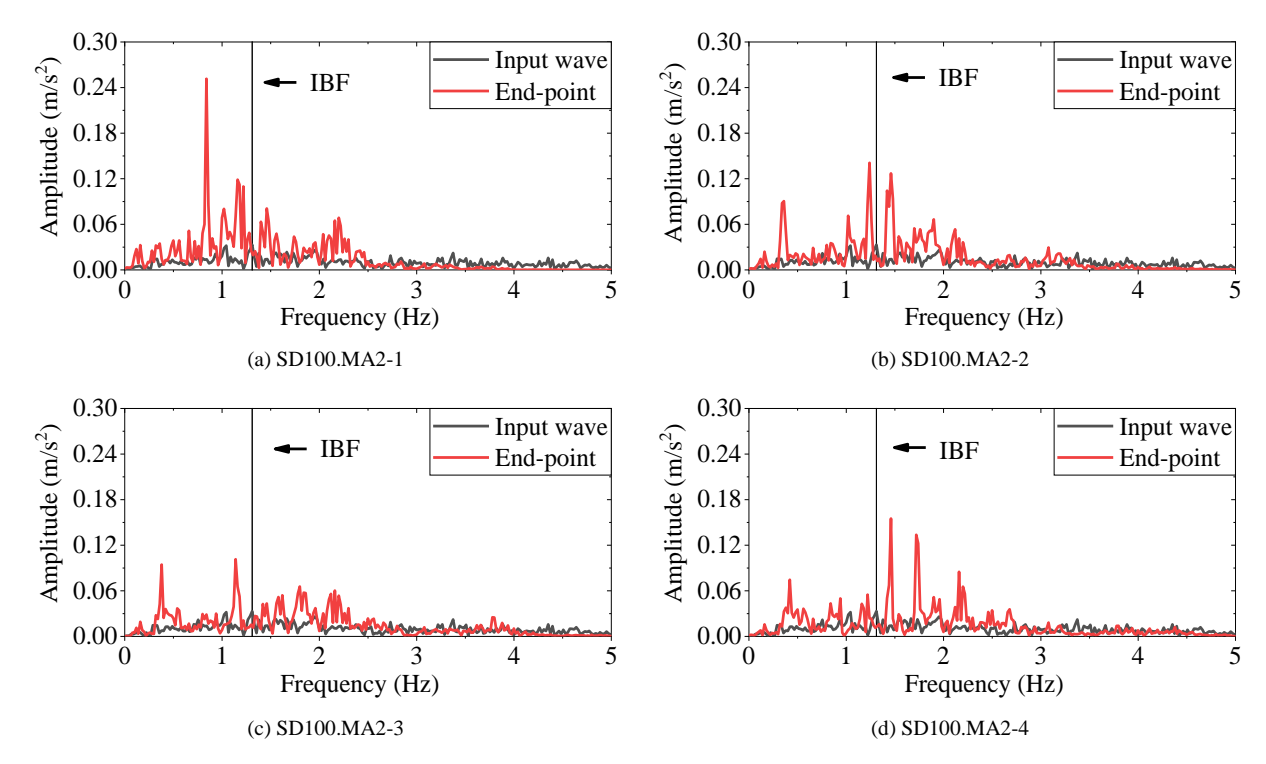


Figure 18. Comparison of acceleration spectra between input wave and left endpoint

5. Topographic and Geological Effect of 3D Simulation

5.1. Three-Dimensional Simulation Model

Real topographic and geological conditions are more complex than ideal ones. In addition, the 3D model added a horizontal vibration in one direction to the 2D model, which complicated the earthquake response in mountainous regions. To explore the ground motion amplification effect on a real mountain terrain, a 3D model of the MOXI platform was built using digital elevation model data, as shown in Figure 19. The size of the area was 3600×3600 m, and the height difference was 1302 m. The thicknesses of the first and second geological layers were 100 and 200 m, respectively. Viscoelastic artificial boundaries were built in different geological layers according to the different rock—soil properties.

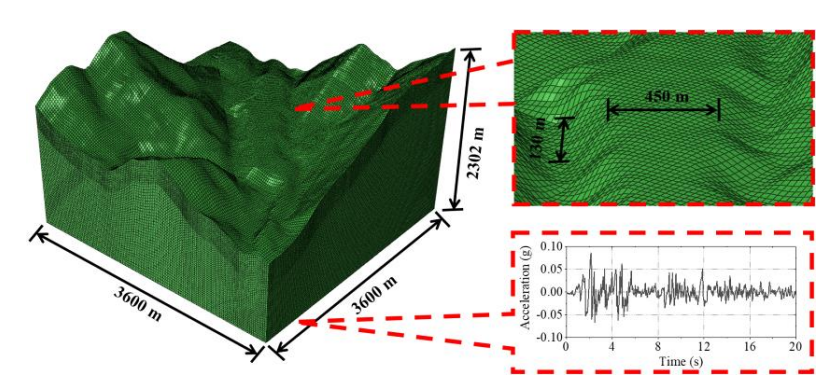


Figure 19. Model size and acceleration time-history curve of earthquake wave

Considering the calculation accuracy and efficiency, through extensive trial calculations, it was decided to adopt a mesh with a size of 25 m. The mesh size met the criterion that it should be less than 1/10 to 1/8 of the minimum wavelength of the input seismic wave [28]. The model contained 1,036,800 elements. Four 3D models were designed, as shown in Figure 20. Figures 20-a to 20-c show the comparison models of different geological layers, and Figure 20(d) shows the comparison models of the three layers with different rock—soil properties. For computational efficiency, the duration of the input seismic wave was shortened to 20 s, including the peak acceleration (0.086g), as shown in Figure 19. It was necessary to ensure that the frequency band where the seismic wave energy was concentrated during the shortening process was the same as the frequency band where the seismic wave energy was concentrated in the normal case. Earthquake waves were input in the X- and Y-directions, and the ratio was 1:1.

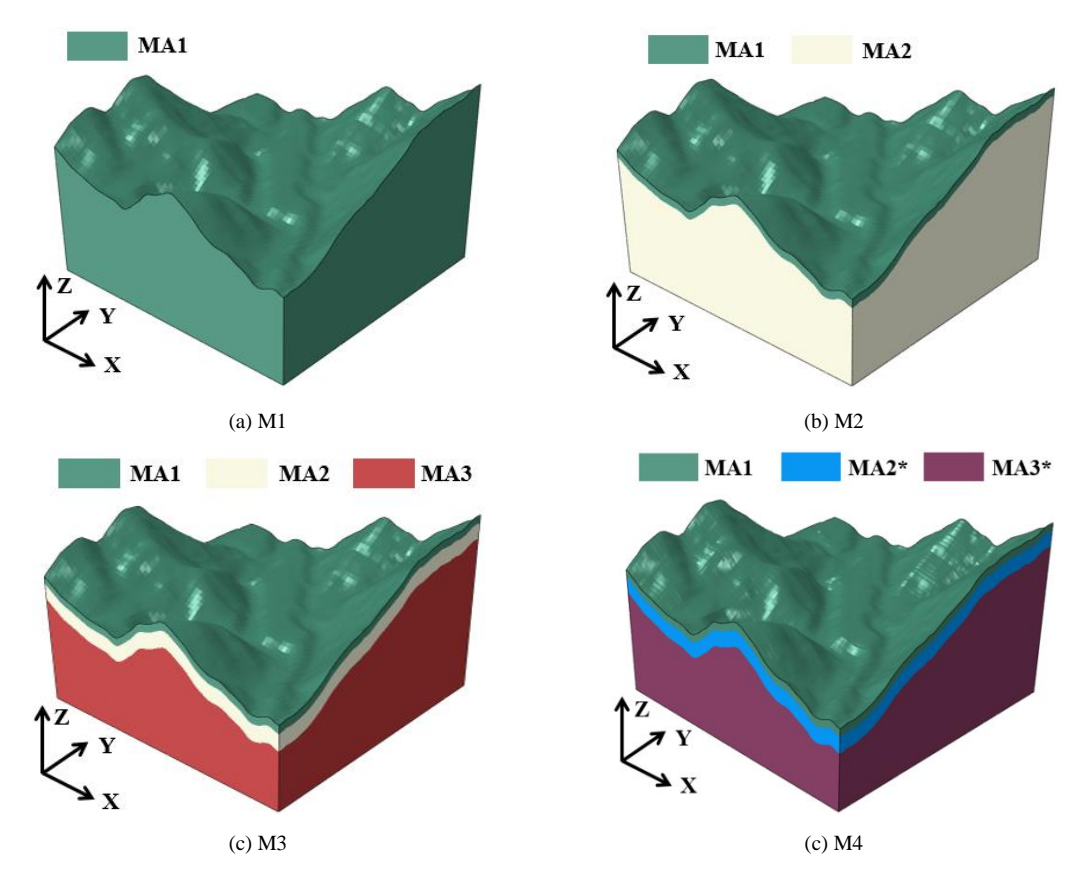


Figure 20. Three-dimensional model with different geological layers

According to the literature by Pan et al. [29], the underground geology of the MOXI platform is lithological. Its material density ρ is 2300 kg/m³, its Young's modulus E is 1.29×1010 N/m², its shear modulus G is 5.18×109 N/m², and its Poisson's ratio ν is 0.25. The P-wave and S-wave velocities are 2118.2 and 1497.8 m/s, respectively, as shown in Table 4. Considering the inhomogeneity of soil, four soil properties(MA2, MA2*, MA3, and MA3*) were added to analyze the influence of geological parameters on the ground motion amplification factor.

Table 4. Geological properties

Material	Geological properties						
	Young's modulus E (kPa)	P-wave velocity V _P (m/s)	S-wave velocity Vs (m/s)	Density ρ (kg/m³)	Poisson's ratio μ		
MA1	2.391e5	323.3	228.6	1830	0.25		
MA2	1.29e7	2118.2	1497.8	2300	0.25		
MA2*	1.935e7	2539.7	1795.8	2400	0.25		
MA3	1.935e7	2539.7	1795.8	2400	0.25		
MA3*	2.58e7	2873.3	2031.7	2500	0.25		

Notes: P-wave velocity is $((\mu + 2 * G)/\rho)^{0.5}$; S-wave velocity is $(G/\rho)^{0.5}$; G is shear modulus and is $0.5 * E/(1 + \mu)$.

5.2. Analysis Results

5.2.1. Comparison of Earthquake Wave Transmission

As listed in Table 4, the seismic wave velocities differed, resulting in different surface vibrations. Figure 21 shows the acceleration cloud images of the four specimens at different times. M1 had the weakest seismic response among the four specimens, and there were no surface sites with accelerations greater than 3 m/s². By contrast, the other three specimens had sites greater than 5 m/s² at 4.0 s. This indicates that the seismic response of the platform improved significantly when the bedrock was considered. Compared with the specimens with bedrock layers, the surface of the ground vibrated first because of the higher propagation velocity of the bedrock of M4. The type of bedrock had an obvious influence on the ground motion of the platform.

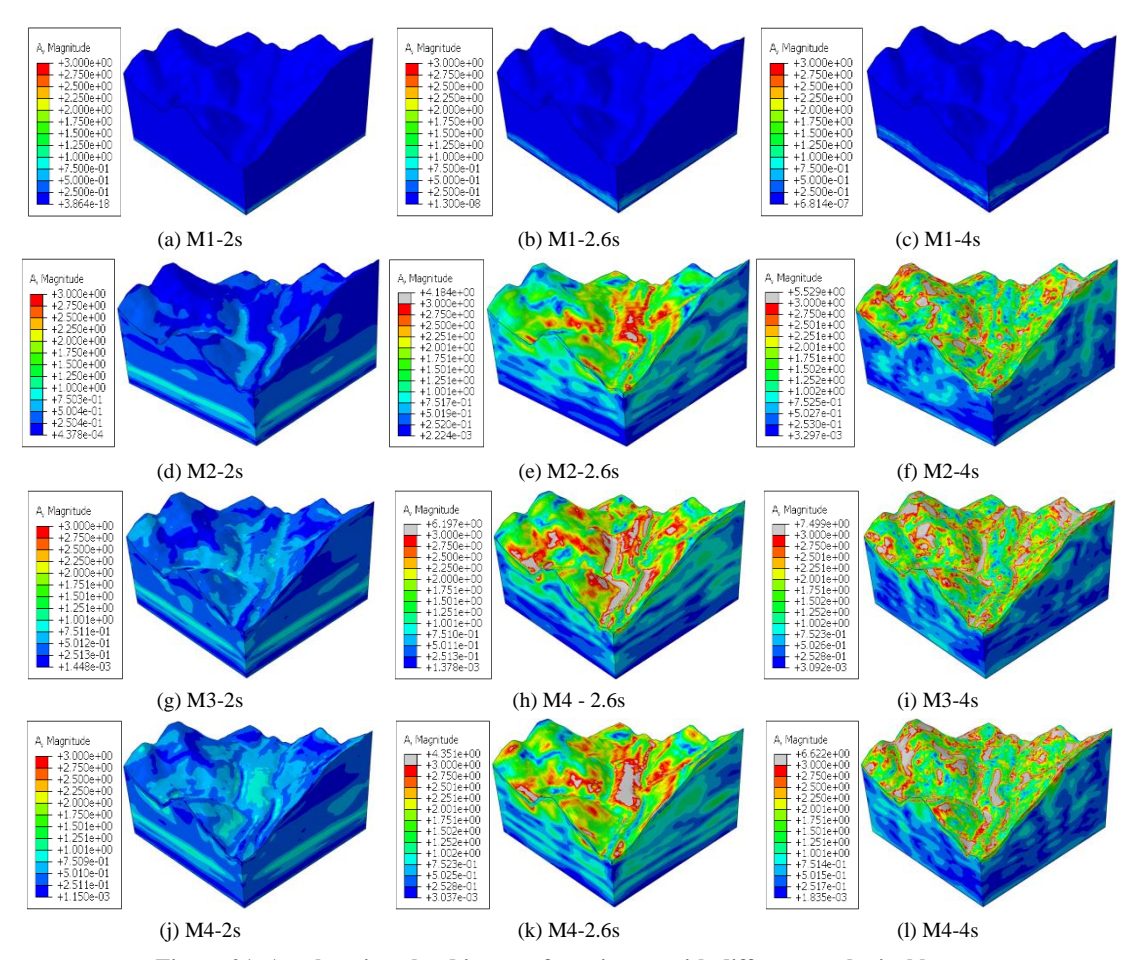
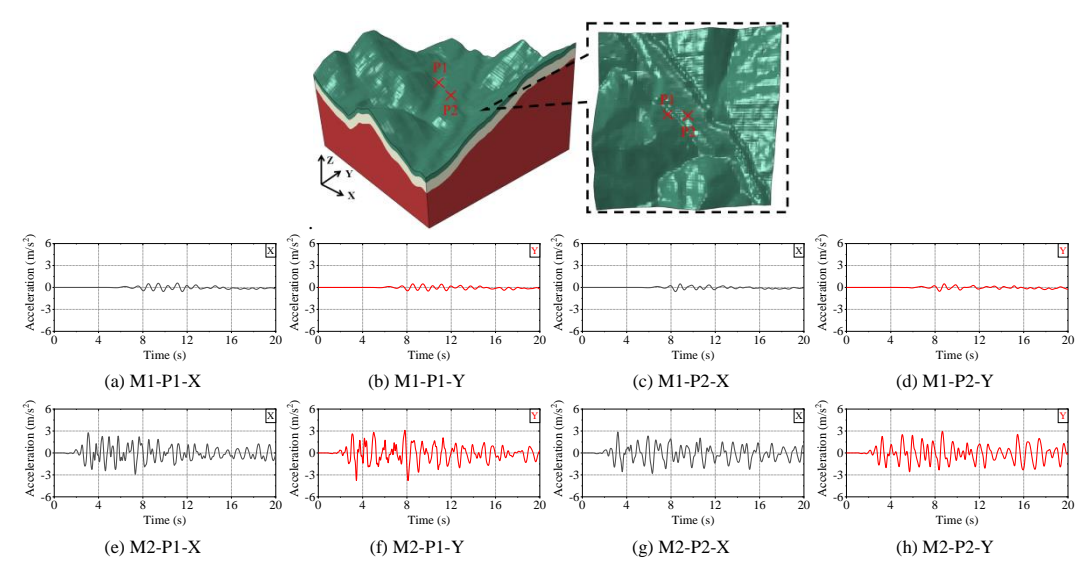


Figure 21. Acceleration cloud image of specimens with different geological layers

5.2.2. Comparison of Acceleration Time-History at Measured Points with Different Locations

The acceleration time-history curves of the bottom and surface of the platform were extracted, as shown in Figure 22, where P1 and P2 are the bottom and surface of the platform, respectively. Although the input seismic waves were the same, the accelerations of P1 and P2 in Specimen 1 were significantly lower than those of the other specimens. This indicates that the soil and rock geology had an obvious influence on the propagation of seismic waves. The magnitude of the acceleration also differed between the two directions. For example, the maximum accelerations of the P2 of Specimen 3 were 4.61 and 3.20 m/s² in the X- and Y-directions, respectively. For the upper surface of the MOXI platform, the seismic response in the X-direction was more pronounced. In addition, for the three specimens that considered the bedrock, the properties of the bedrock influenced the propagation of seismic waves, and this influence was nonlinear with an increase in the Young's modulus of the bedrock. For example, the maximum accelerations of P2 in the X-direction were 2.86, 4.61, and 3.41 m/s² for M2, M3, and M4, respectively. This improved the complexity of the research on mountain ground motion.



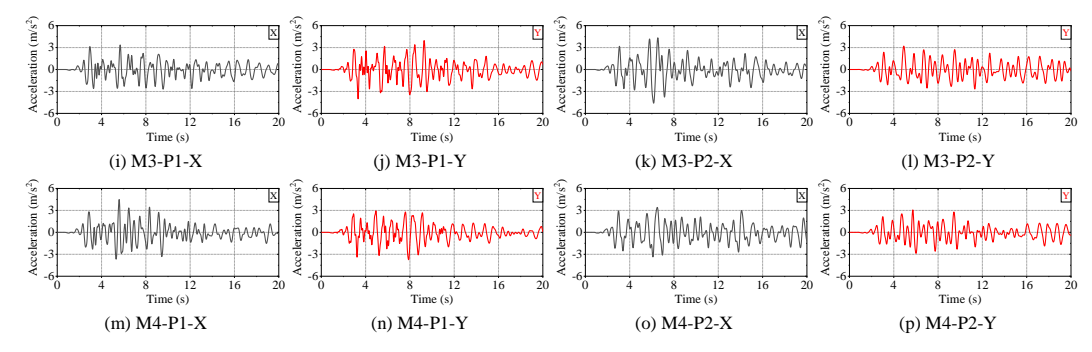


Figure 22. Acceleration time-history curves of specimens with different sites

Figure 23 shows the Fourier spectrum of the acceleration time-history curve. The spectrum curve reveals that the amplifications of the specimens with bedrock were mainly concentrated at a high frequency (greater than the base frequency of the input wave, 1.31 Hz), and the amplification factor was greater than 5. This was because the bedrock was more sensitive to high-frequency waves and could more easily propagate high-frequency seismic waves.

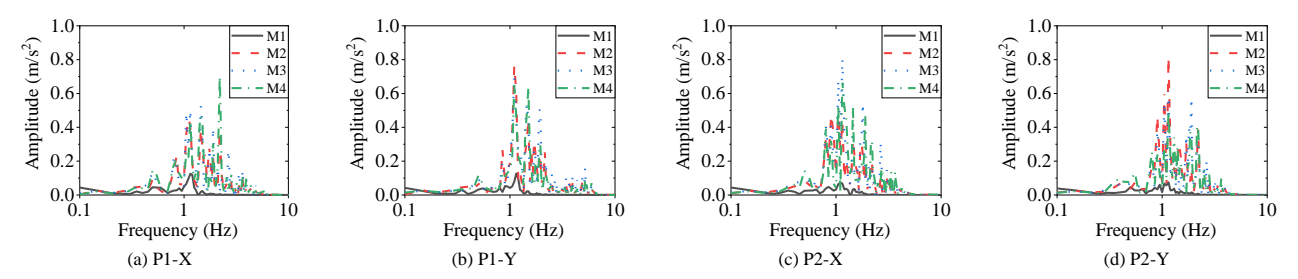


Figure 23. Fourier spectrum of the acceleration time-history curve

5.2.3. Comparison of Acceleration Time-History at Measured Points with Different Depths

Figure 24 shows the acceleration time-history curves of the soil cover layer at different depths. The acceleration time-history curves at the top and bottom of the soil cover layer differ significantly. The peak acceleration at the bottom of the soil cover layer was much smaller than that at the top, indicating that the ground motion amplification effect was concentrated mainly in the soil cover layer for the topographic model considering bedrock. Compared with the bottom of the soil cover layer, although the types of bedrock differed, they had a minor influence on the acceleration time-history curve at P2.

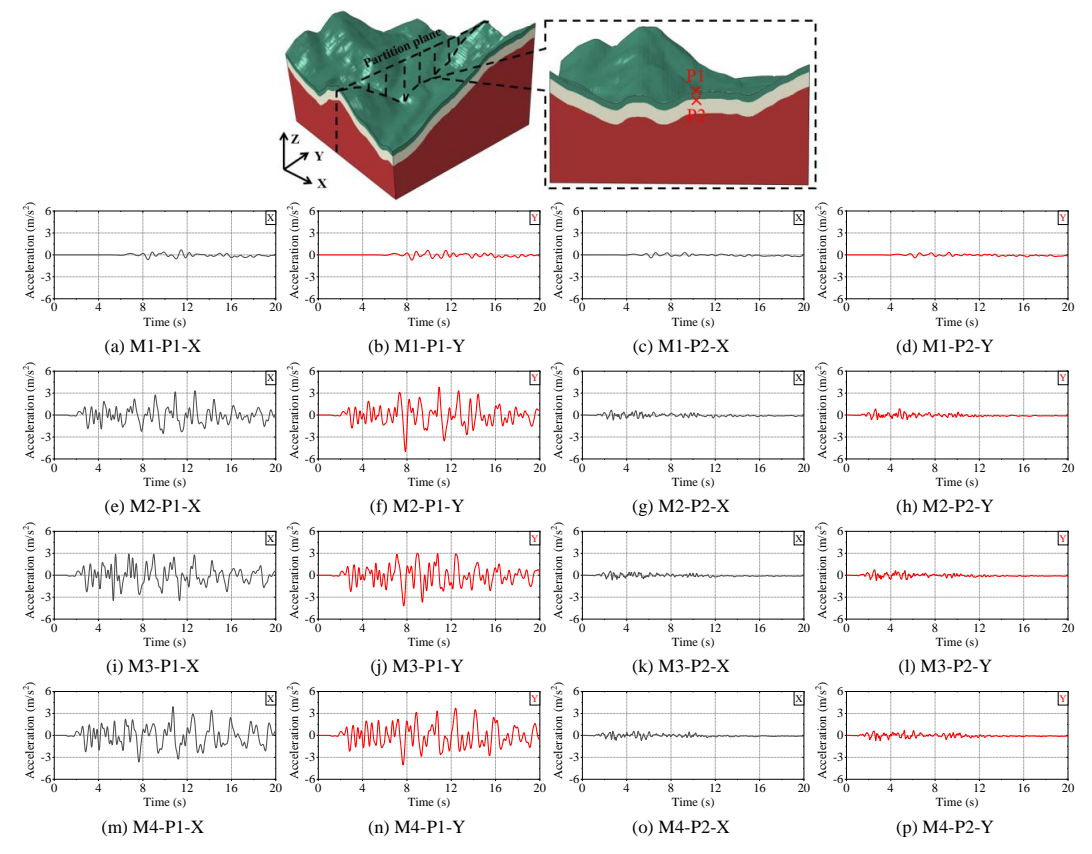


Figure 24. Acceleration time-history curves of specimens with different depths

Figure 25 shows a comparison of the Fourier spectral curves of the P1 and P2 accelerations in the four specimens. At the bottom of the soil cover layer, the seismic acceleration was dominated by high-frequency waves, with a maximum acceleration amplitude not exceeding 0.1 m/s². The acceleration amplitude increased when passing through the soil cover layer. Simultaneously, the frequency of the amplification region changed from high to low owing to the filtering of the soil layer, which was consistent with previous studies. In summary, the amplification of ground motion by the soil cover layer is one of the main causes of more-severe disaster damage in mountainous areas under complex geological conditions.

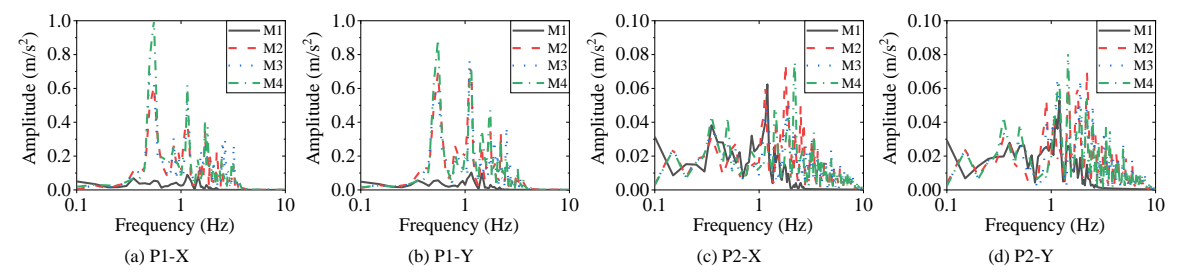


Figure 25. Fourier spectra of the acceleration time-history curves

5.2.4. Comparison of Surface Ground Motion Amplification Factors

Figure 26 shows the acceleration amplification effects of four specimens with different geological layers in different directions, where "M," "X," and "Y" represent the acceleration vector direction, X-direction, and Y-direction, respectively. With an increase in the number of geological layers, the amplification effect of the platform topography became more obvious (the value of the amplification factor also increased). For example, the ground motion amplification factor was mainly less than 1.5 for the single-layer platform M1, while the maximum topographic amplification factor exceeded 5 for the multilayer platforms M2, M3, and M4. Platforms with the same geological conditions exhibited different topographic effects in different directions. The main reason may be that different topographic cross sections in different directions affected the ground motion amplification effect.

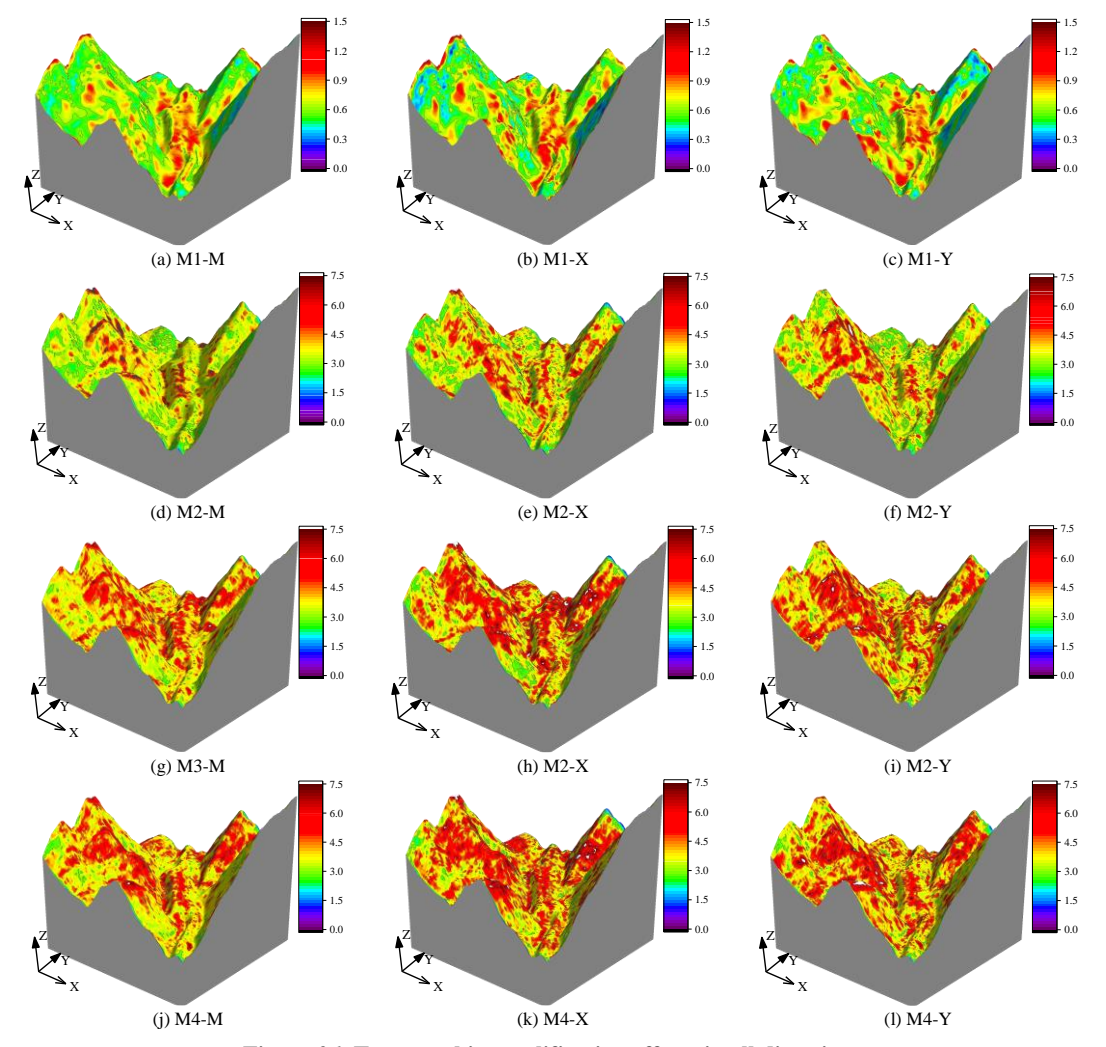


Figure 26. Topographic amplification effects in all directions

Local magnification of M4-M was performed to explore the topographic effects of the platform surface further, as shown in Figure 27. There was an obvious amplification of the ground motion in the platform area, and the amplification effect was most pronounced at the edge and in the middle of the platform. In Zones 1 and 2, the amplification factors were 3.52 and 5.53, respectively. This was mainly caused by the time lag and phase difference of the scattered waves generated at the platform after reaching the surface of the platform. However, the superposition effect of the scattered and incident waves at the edge of the platform was more likely to occur, leading to an amplification of the ground motion. In addition, the ground motion amplification factor in Zone 3 was 6.45, indicating that a strong earthquake region might exist in the middle of the platform.

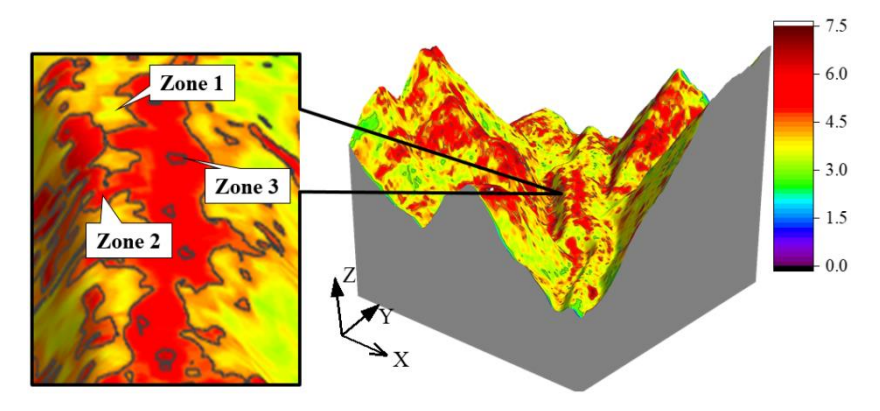


Figure 27. Topographic amplification effect of M4 in the x direction

6. Modified Ground Motion Amplification Factor

The provisions of the Chinese seismic code on the ground motion amplification factor of the platform topography were not safe (the ground motion amplification factor resulting from topographic and geological effects easily exceeded 1.6 in real situations), indicating that the provisions needed modification. In addition, according to this study, the height of the platform, width of the upper surface, angle of the platform apex (angle between the surface inclination and the slope of the platform), and geological parameters all had influences. Hence, the effects of these parameters should be included in the formula. The reference expression for the ground motion amplification factor summarizes the simulation results of this study, as shown in Equation 5.

$$\lambda = 1 + \xi \eta \gamma \alpha \tag{5}$$

where λ is the ground motion amplification factor of platform topography, α is the influence coefficient considering the platform height, ξ is the influence coefficient considering the surface width of the platform. η is the influence coefficient considering the platform apex, and γ is the influence coefficient considering the different uniform geological condition, which can be used to perform interpolation calculation based on P-wave velocity. The values of the influence coefficients are listed in Table 5. When the parameters exceed the ranges in Table 5, the platform topography must be analyzed in detail to obtain the ground motion amplification factor. The topographies with mixed geological layers are not within this range.

	Height (m)	α	Width (m)	ξ	Angle (°)	η	Geological type	γ
	0	0	0	1.0	150	1.0		0.95
H Angle Geological type	25	0.1	25	1.25	145	1.03	Soft subsoil	
	50	0.2	50	1.5	140	1.05		
	75	0.3	75	1.75	135	1.08		
	100	0.4	100	2.0	130	1.10		1.35
	125	0.5	125	2.0	125	1.13	Rocky subsoil	
	150	0.6	150	2.0	120	1.15		

Table 5. Modified increase amplitude of raised topography

To explain the feasibility of the modified increase in amplitude, a comparison of the peak amplification factor between the actual and suggested values was performed, as shown in Table 6. The actual and suggested values were similar, and the average error was 0.19, indicating that the error was within the acceptable range. In addition, for terrain with steeper slopes (60-2.5), the topography parameter was beyond the value range; thus, the suggested value of the amplification factor was not safe. Overall, the suggested value was greater than the actual value, ensuring the safety of the seismic design of mountain structures and providing reference value. Further research will require more samples to verify, refine, and correct the formula.

Source Object α η λ_{R} e 100-150 0.4 2.0 1.10 0.95 1.79 1.84 0.05 0.6 2.0 2.04 2.25 150-150 1.10 0.95 0.21 0.6 200-50 1.5 1.10 0.95 1.54 0.40 1.94 This paper 36-2.5 0.4 2.0 1.05 0.95 1.75 1.80 0.05 45-7.5 0.4 2.0 1.12 0.95 1.70 1.85 0.15 60-2.5 0.4 2.0 1.15 0.95 2.27 1.87 -0.40Profile A 0.6 2.0 1.00 1.2* 2.12 2.44 0.32 Zhou et al. [30] Profile B 0.6 2.0 1.00 1.2* 1.94 2.44 0.50 50gal-110 m thickness 0.5 2.0 1.08 0.95 2.05 2.03 -0.02Wang et al. [31] 200gal-50 m thickness 0.2 2.0 1.08 0.95 1.53 1.41 -0.12Zhang et al. [32] Figure 3-sharp corner-crest 0.2 2.0 1.00 0.95 1.27 1.38 0.11

Table 6. Comparison of peak amplification factors between actual and suggested values

Notes: "*" represents interpolation value according to P-wave velocity. "-" represents average value due to the lack of related data. λ_R and λ_M are the amplification factors of actual value and modified suggested value, respectively. e is the difference between actual value and modified suggested value

7. Conclusions

- During the Luding Ms 6.8 earthquake, two structurally identical frames of the MOXI museum sustained varying degrees of damage. According to the Chinese seismic code, both frame structures were assigned identical ground motion amplification factors of 1.6. This discrepancy indicated that the current specification in the Chinese code regarding platform ground motion amplification factors may be inaccurate and warrant revision to reflect real-world seismic behavior better.
- Prominent local topographic features (such as platform terrains) and complex geological conditions (including
 soft-hard interlayers) significantly interfere with the propagation of seismic waves. These topographic and
 geological characteristics not only alter the original propagation paths of seismic waves, causing them to focus or
 diverge, but also generate complex wavefield superposition effects through multiple reflections and refractions at
 stratigraphic interfaces. As a result, the ground motion at the surface exhibits strong spatial heterogeneity.
- The height, width, surface angle, and slope of the platform influenced the value of the ground motion amplification factor of the platform by modifying the paths, reflection, and resonance of the earthquake wave. The maximum ground motion amplification factor on the platform surface did not necessarily appear at the peak of the platform, such as in specimens 200-150, because of intricate wave superposition and interference effects.
- Soil layers with a low elastic modulus act as filters, selectively attenuating high-frequency seismic waves, whereas those with a high elastic modulus are more prone to amplifying such waves. A soil depth within 200 m exerts minimal influence on the ground motion amplification factor. Moreover, a soil layer interface exhibiting a Mode 1 shape facilitates superior seismic wave propagation, thereby resulting in a higher ground motion amplification factor under Mode 1 conditions.
- The vibration intensity experienced by the platform is significantly influenced by the varying impacts of distinct geological strata on seismic wave propagation. Moreover, for platforms resting on mixed geological layers, the amplification effect of the seismic waves is enhanced significantly, occurring predominantly within the overlying soil layer. This amplification effect gradually diminishes as the depth beneath the surface increases.
- Based on the findings of this study, the ground motion amplification factor for the platform has been revised, with its feasibility substantiated through a comparative analysis of the actual measured and the newly proposed values. The results unequivocally demonstrate that the adjusted amplification factor can improve structural design practices, enhancing the safety performance of buildings in mountainous regions.

8. Declarations

8.1. Author Contributions

Conceptualization, Q.L. and Y.T.; methodology, Q.L. and Y.L.; software, Q.L. and M.Z.; formal analysis, Q.L.; investigation, Q.L.; resources, S.Z. and J.X.; data curation, S.Z.; writing—original draft preparation, Q.L.; writing—review and editing, J.X.; supervision, Y.T.; funding acquisition, J.X. All authors have read and agreed to the published version of the manuscript.

8.2. Data Availability Statement

The data presented in this study are available on request from the corresponding author.

8.3. Funding

The authors are grateful for the financial support received from the Science & Technology Department of Sichuan Province [grant number 2024JDRC0101], Key Research and Development Project of Chengdu [No. 2025-YF05-00440-SN], Research Project of Sichuan Architectural Design and Research Institute [KYYN2025020 and KYYN2025018], and the Open Fund of the Sichuan Engineering Research Center for Mechanical Properties and Engineering Technology of Unsaturated Soils [grant numbers SC-FBHT2024-05].

8.4. Conflicts of Interest

The authors declare no conflict of interest.

9. References

- [1] Li, S. Q., & Chen, Y. S. (2024). Seismic risk estimation of composite structures considering improved vulnerability levels. Structures, 65, 106645. doi:10.1016/j.istruc.2024.106645.
- [2] Lopes, G. C., Silva, V., Costa, C., Vicente, R., & Oliveira, C. S. (2024). Advancing the understanding of earthquake risk in Portugal. Bulletin of Earthquake Engineering, 22(11), 5379–5401. doi:10.1007/s10518-024-01975-0.
- [3] FathiAzar, A., De Angeli, S., & Cattari, S. (2024). Towards integrated multi-risk reduction strategies: A catalog of flood and earthquake risk mitigation measures at the building and neighborhood scales. International Journal of Disaster Risk Reduction, 113, 104884. doi:10.1016/j.ijdrr.2024.104884.
- [4] Bhadauria, P. K. S. (2024). Comprehensive review of AI and ML tools for earthquake damage assessment and retrofitting strategies. Earth Science Informatics, 17(5), 3945–3962. doi:10.1007/s12145-024-01431-2.
- [5] Manzunzu, B., Midzi, V., Zulu, B., Mulabisana, T., Pule, T., Sethobya, M., & Mankayi, N. (2025). Site response analysis for estimation of seismic site amplification in the city of Durban (South Africa). Natural Hazards Research, 5(1), 219–228. doi:10.1016/j.nhres.2024.11.002.
- [6] Zhou, H. (2025). Multi-parameter modeling and analysis of ground motion amplification in the Quaternary sedimentary basin of the Beijing-Tianjin-Hebei region. Earthquake Science, 38(2), 136–151. doi:10.1016/j.eqs.2024.11.002.
- [7] NEES-2010-0977. (2012). Topographic effects in strong ground motion from physical and numerical modeling to design. Network for Earthquake Engineering Simulation (NEES), West Lafayette, United States. Available online: https://www.designsafe-ci.org/data/browser/public/nees.public/NEES-2010-0977 (accessed on August 2025).
- [8] Pelekis, P., Batilas, A., Pefani, E., Vlachakis, V., & Athanasopoulos, G. (2017). Surface topography and site stratigraphy effects on the seismic response of a slope in the Achaia-Ilia (Greece) 2008 Mw6.4 earthquake. Soil Dynamics and Earthquake Engineering, 100, 538–554. doi:10.1016/j.soildyn.2017.05.038.
- [9] Dhabu, A. C., & Gudimella, R. S. T. (2021). Influence of Himalayan topography on earthquake ground motions. Arabian Journal of Geosciences, 14(18), 1931. doi:10.1007/s12517-021-08111-1.
- [10] Hartzell, S., Meremonte, M., Ramirez-Guzman, L., & McNamara, D. (2013). Ground Motion in the Presence of Complex Topography: Earthquake and Ambient Noise Sources. Bulletin of the Seismological Society of America, 104(1), 451–466. doi:10.1785/0120130088.
- [11] Luo, Y., Fan, X., Huang, R., Wang, Y., Yunus, A. P., & Havenith, H. B. (2020). Topographic and near-surface stratigraphic amplification of the seismic response of a mountain slope revealed by field monitoring and numerical simulations. Engineering Geology, 271, 105607. doi:10.1016/j.enggeo.2020.105607.
- [12] Glinsky, N., Bertrand, E., & Régnier, J. (2019). Numerical simulation of topographical and geological site effects. Applications to canonical topographies and Rognes hill, South East France. Soil Dynamics and Earthquake Engineering, 116, 620–636. doi:10.1016/j.soildyn.2018.10.020.
- [13] Hough, S. E., Altidor, J. R., Anglade, D., Given, D., Janvier, M. G., Maharrey, J. Z., Meremonte, M., Mildor, B. S. L., Prepetit, C., & Yong, A. (2010). Localized damage caused by topographic amplification during the 2010 M7.0 Haiti earthquake. Nature Geoscience, 3(11), 778–782. doi:10.1038/ngeo988.
- [14] Shen, H., Liu, Y., Li, X., Li, H., Wang, L., & Huang, W. (2025). The combined amplification effects of topography and stratigraphy of layered rock slopes under vertically and obliquely incident seismic waves. Soil Dynamics and Earthquake Engineering, 193, 109331. doi:10.1016/j.soildyn.2025.109331.
- [15] GB 50011-2010. (2016). Code for seismic design of buildings. China Architecture & Building Press, Beijing, China. (In Chinese).
- [16] Zhang, L., Fu, L., Liu, A., & Chen, S. (2023). Simulating the strong ground motion of the 2022 MS6.8 Luding, Sichuan, China Earthquake. Earthquake Science, 36(4), 283–296. doi:10.1016/j.eqs.2023.05.001.

- [17] Zhang, S., Wu, Z., & Zhang, Y. (2023). Is the September 5, 2022, Luding MS6.8 earthquake an 'unexpected' event? Earthquake Science, 36(1), 76–80. doi:10.1016/j.eqs.2023.02.004.
- [18] Yuan, Z., Zhao, J., Huang, Y., Yu, H., Niu, A., Ma, H., & Ma, L. (2023). Study on deformation characteristics and dynamic cause of the Luding M S6.8 earthquake. Frontiers in Earth Science, 11, 1232205. doi:10.3389/feart.2023.1232205.
- [19] Zhou, J., Xi, N., Kang, C., Li, L., Chen, K., Tian, X., Wang, C., & Tian, J. (2023). An accessible strong-motion dataset (PGA, PGV, and site vS30) of 2022 MS6.8 Luding, China Earthquake. Earthquake Science, 36(4), 309–315. doi:10.1016/j.eqs.2023.01.001.
- [20] Liu, X., Su, P., Li, Y., Xia, Z., Ma, S., Xu, R., Lu, Y., Li, D., Lu, H., & Yuan, R. (2023). Spatial distribution of landslide shape induced by Luding Ms6.8 earthquake, Sichuan, China: case study of the MOXI Town. Landslides, 20(8), 1667–1678. doi:10.1007/s10346-023-02070-2.
- [21] Song, X., Cao, T., Gao, P., & Han, Q. (2020). Vibration and damping analysis of cylindrical shell treated with viscoelastic damping materials under elastic boundary conditions via a unified Rayleigh-Ritz method. International Journal of Mechanical Sciences, 165, 105158. doi:10.1016/j.ijmecsci.2019.105158.
- [22] Peng, Y., Zhao, J., Sepehrnoori, K., & Li, Z. (2020). Fractional model for simulating the viscoelastic behavior of artificial fracture in shale gas. Engineering Fracture Mechanics, 228, 106892. doi:10.1016/j.engfracmech.2020.106892.
- [23] Liu, X., Chen, J., Zhao, Z., Lan, H., & Liu, F. (2018). Simulating Seismic Wave Propagation in Viscoelastic Media with an Irregular Free Surface. Pure and Applied Geophysics, 175(10), 3419–3439. doi:10.1007/s00024-018-1879-9.
- [24] Jing-bo, L. I. U., Zhen-yu, W. A. N. G., Xiu-Li, D. U., & Yi-Xin, D. U. (2005). Three-dimensional visco-elastic artificial boundaries in time domain for wave motion problems. Engineering Mechanics, 22(6), 46-51.
- [25] Zhao, S., Luo, Q., Zhang, M., Xiong, F., & Yang, S. (2023). Numerical analysis of ground motion amplification coefficient under complex topography. Structures, 58, 105353. doi:10.1016/j.istruc.2023.105353.
- [26] Sun, Z., Kong, L., Guo, A., Xu, G., & Bai, W. (2019). Experimental and numerical investigations of the seismic response of a rock–soil mixture deposit slope. Environmental Earth Sciences, 78(24), 1–14. doi:10.1007/s12665-019-8717-y.
- [27] Huang, D., Sun, P., Jin, F., & Du, C. (2021). Topographic amplification of ground motions incorporating uncertainty in subsurface soils with extensive geological borehole data. Soil Dynamics and Earthquake Engineering, 141, 106441. doi:10.1016/j.soildyn.2020.106441.
- [28] Kuhlemeyer, R. L., & Lysmer, J. (1973). Finite Element Method Accuracy for Wave Propagation Problems. Journal of the Soil Mechanics and Foundations Division, 99(5), 421–427. doi:10.1061/jsfeaq.0001885.
- [29] Pan, Y. Ren, J. Ren, Y. Zhao, J. & Ba, Z. (2023). Seismic damage investigation and analysis of a frame structure in the Luding Ms6.8 earthquake with platform effect." China Civil Engineering Journal, 23050358. doi:10.15951/j.tmgcxb.23050358.
- [30] Zhou, H., Li, J., & Chen, X. (2020). Establishment of a seismic topographic effect prediction model in the Lushan Ms 7.0 earthquake area. Geophysical Journal International, 221(1), 273–288. doi:10.1093/gji/ggaa003.
- [31] Wang, L., Wu, Z., Xia, K., Liu, K., Wang, P., Pu, X., & Li, L. (2019). Amplification of thickness and topography of loess deposit on seismic ground motion and its seismic design methods. Soil Dynamics and Earthquake Engineering, 126, 105090. doi:10.1016/j.soildyn.2018.02.021.
- [32] Zhang, Z., Fleurisson, J. A., & Pellet, F. (2018). The effects of slope topography on acceleration amplification and interaction between slope topography and seismic input motion. Soil Dynamics and Earthquake Engineering, 113, 420–431. doi:10.1016/j.soildyn.2018.06.019.